Wind Dynamics of Cygnus X-1

1 October 2011

Andreas Glossner
supervised by
Dr. Manfred Hanke and Prof. Dr. Jörn Wilms

**Dr. Karl Remeis-Sternwarte and
Erlangen Centre for Astroparticle Physics**

Friedrich-Alexander-Universität Erlangen-Nürnberg

**Friedrich-Alexander-Universität
Erlangen-Nürnberg**

Contents

Abstract

In this project, the wind dynamics of the X-ray binary system Cygnus X-1/ HDE 226868 was studied through a simulation. In a first step, the motion of particles in the gravitational potential of the compact object and the companion star was calculated. This model was then gradually extended to take into account the star's radiative pressure as well as photoionization. Amongst other things, it was found that in the simulation, the fraction of accreted wind particles is approximately high enough to explain the X-ray luminosity of the black hole candidate if the ionization area extends roughly to the supergiant's surface.

1 Background

1.1 X-Ray Binaries

X-ray binaries consist of a compact object and a companion star, the earlier of which emits strong radiation in the X-ray regime. The compact object can be either a black hole, a neutron star, or a white dwarf. X-ray binaries are among the brightest X-ray sources on the sky, mainly drawing their power from a process called accretion. Large amounts of gravitational energy are released by material falling from the companion star (i.e. donor) onto the accretor. The analysis of the ionizing radiation stemming from this process then makes it possible to evaluate properties of the compact object itself (e.g., Schatz & Rehm, 2006).

The compact objects in X-ray binaries are remnants of stellar evolution: If a star's core has a mass below $1.44\,M_\odot$ (Chandrasekhar limit) left after the ejection of its outer layers, it becomes a white dwarf. It contracts until stabilized by the degeneracy pressure of atomic electrons. Stars with more massive remnants (possibly after a supernova explosion) form either neutron stars or black holes, depending on the final mass. If the Oppenheimer-Volkoff limit around $2-3\,M_\odot$ is exceeded, the object contracts to become a black hole; for masses below that limit a neutron star can develop, stabilized by the degeneracy pressure of neutrons (Janka et al., 2001).

1.2 Accretion in X-Ray Binaries

Several mechanisms may allow for the accretion process onto compact objects, though the detailed physics behind this process has not been entirely understood yet (Frank et al., 2002; Kühnel, 2011).

In a first process called *Roche lobe overflow*, material moves into the gravitational potential of the compact object due to an expansion of the companion star or because of a decrease in the binary distance (Kühnel, 2011). The Roche potential is given by

$$\phi_{\mathrm{R}}(\mathbf{r}) = -G\frac{M_1}{|\mathbf{r}-\mathbf{r}_1|} - G\frac{M_2}{|\mathbf{r}-\mathbf{r}_2|} - \frac{1}{2}(\omega\times\mathbf{r})^2 \qquad (1.1)$$

where M_1 and M_2 are the masses of the binary components and $\mathbf{r}$ is a vector pointing away from the system's center of mass. The potential is approximately spherically symmetric close to the centers of the two binary components, but further outside it is distorted along the axis connecting the two centers (Frank et al., 2002). In the case of a binary, five so-called Lagrangian points L_1 - L_5 exist, in which an object (with a mass much smaller than the binary masses) may stay at rest with regard to the co-rotating coordinate system.

In a second process, the companion star is emitting mass through *stellar winds*, parts of which are then accreted by the compact object. Usually the donor is an early-type star

(O or B), launching winds at velocities around

$$v_{\text{escape}} = \sqrt{\frac{2GM_p}{R_p}} \approx 10^3 \, \text{km s}^{-1} \tag{1.2}$$

(Israel, 1996, also see section 2 of this project report).

A third possibility is *accretion from Be stars*. Rapidly rotating B stars lose equatorial mass in irregular intervals, a fraction of which may be accreted by the companion (Israel, 1996).

1.3 Cygnus X-1

1.3.1 General Properties

The simulation in the following will be performed at the example of the famous X-ray binary system Cygnus X-1. It has been discovered in a rocket flight experiment in 1964 (Bowyer et al., 1965), with its position being narrowed down to $\lesssim 5''$ in subsequent years (see Hanke, 2011, for an historical overview). In 1972, the discovered X-ray source was identified with the O9.7 Iab supergiant star HDE 226868 (Bolton, 1972; Webster & Murdin, 1972), triggering intensive research of Cygnus X-1 because of indications that the X-ray source might be a black hole with stellar masses, i.e., several $M_\odot$ (e.g., Gies et al., 2003).

The analysis of the optical observation data by Bolton (1972), indicating a period of $\approx 5.6 \, \text{d}$, set the lower mass-limit of the compact object at $3 \, M_\odot$ and suggested that it might be a black hole. This assumption has since been corroborated by further evidence (see e.g., Cowley, 1992).

A number of different values have been given in literature for the orbital inclination i of the system. Herrero et al. (1995) state that

$$i = 35° \tag{1.3}$$

falls into the center of those literature values and is therefore a reasonable assumption; thus this value was also used throughout this report.

Different determinations of the mass ratio

$$q = \frac{M_{\text{bh}}}{M_\star} \tag{1.4}$$

have been conducted, where M_{bh} and $M_\star$ are the masses of the black hole and the O-star, respectively. Using a model assuming an alignment of the rotational and orbital axes, the mentioned orbital inclination $i = 35°$ and several other assumptions, Herrero et al. (1995) derive $M_{\text{bh}} = 10.1 \, M_\odot$ (Cygnus X-1) and $M_\star = 17.8 \, M_\odot$ (HDE 226868). The mass ratio of

$$q = 0.567 \tag{1.5}$$

thus obtained is used in the following simulation.

1.3.2 Accretion

In Cygnus X-1, accretion is assumed to be partly due to the donor star being close to filling its critical Roche lobe. This causes mass to flow through the inner Lagrangian point L1 towards the black hole. Additionally, the radiatively driven wind from the surface of the supergiant contributes to accretion. A fraction of it is diverted by the gravitational potential of the compact object and is accreted by the same (Gies et al., 2008). A mixture of both of these processes then leads to a "focused wind" (e.g., Friend & Castor, 1982) streaming from the O star towards the black hole.

In the presence of the intense X-ray flux from the compact object, the gas particles driving the wind become strongly ionized (Hanke et al., 2009; Hanke, 2011). If this ionization, decreasing the wind velocity by reducing the driving force of the UV photons onto the wind particles (Blondin, 1994), takes place close to the supergiant, the wind might become too slow to reach the area where the BH's gravitational acceleration is dominating. In this case, the regions at the star's surface which are nearest to the BH would no longer contribute to accretion. However, Gies et al. (2008) mention that the X-ray flux could cause a thermal wind from the outer layers of the star, inducing a mass transfer from there instead.

In the following, each of these effects was successively included into a simulation, albeit often strongly simplified models were used.

2 Simulation

2.1 Fundamentals

The programming was carried out using S-Lang in the Interactive Spectral Interpretation System (ISIS; Houck & Denicola, 2000). A simple two-particle model was implemented and then gradually extended to make the simulation more realistic.

Length and Time Units
In the following, the *length unit* is the distance between black hole (BH) and companion star $a = r_{\mathrm{bh}} + r_\star$, where r_{bh} (BH) and $r_\star$ (supergiant) are the respective distances from the system's center of mass (CM). For Cygnus X-1, $a \sim 40\,R_\odot$, which can be derived from

$$q = \frac{M_{\mathrm{bh}}}{M_\star} = \frac{r_\star}{r_{\mathrm{bh}}}. \tag{2.1}$$

According to Gies et al. (2003), $r_\star \sin i = 8.36(8)\,R_\odot$, while a common assumption for the inclination angle is $i = 35°$, and the mass ratio q is approximately 10.1/17.8 (Equations 1.3 and 1.5). The *time unit* used is the orbital period $P = 5.6\,\mathrm{d}$ (Gies et al., 2008) and the *star's radius* $R_\star$ is assumed as $\sim 17\,R_\odot$ after Herrero et al. (1995).

Making use of the thus defined length unit and q, one gets a convenient expression for the distances r_{bh} and $r_\star$:

$$r_{\mathrm{bh}} = \frac{1}{1+q} \qquad \text{and} \qquad r_\star = \frac{q}{1+q} \tag{2.2}$$

BH and Supergiant Orbits
In contrast to claims from early determinations (e.g., Bolton, 1975), the orbits in Cygnus X-1 do not seem to have a significant eccentricity (Gies & Bolton, 1982). This justifies that throughout the simulation, the motion of the BH and of the center of mass of the supergiant was approximated by circular Kepler orbits.

Let the orbital plane be identical to the xy-plane. Then the motion of BH and star can be described as

$$\mathbf{r}_{\mathrm{bh}} = -\frac{1}{1+q} \begin{pmatrix} \cos 2\pi t \\ \sin 2\pi t \\ 0 \end{pmatrix} \tag{2.3}$$

$$\mathbf{r}_\star = \frac{q}{1+q} \begin{pmatrix} \cos 2\pi t \\ \sin 2\pi t \\ 0 \end{pmatrix}. \tag{2.4}$$

Figure 3 shows the orbital plane in the simulation. Note the large size of the supergiant relative to the BH-star distance.
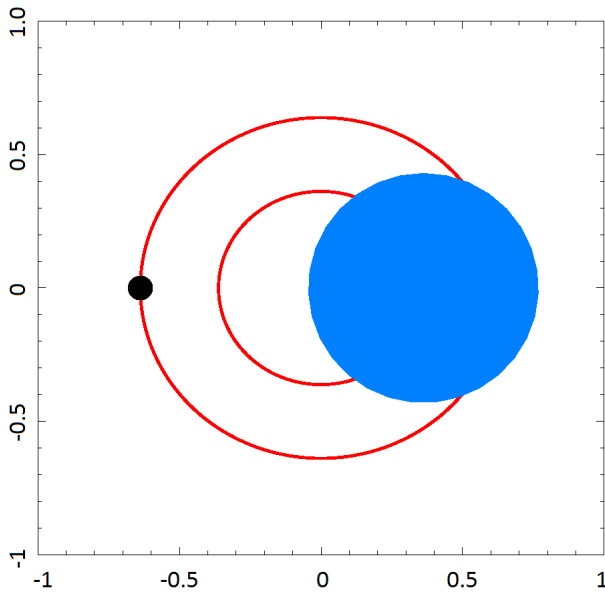
Figure 1: The orbital plane in the simulation (plan view, center of mass at (0,0)). The size of the blue supergiant (blue) is to scale if a radius of $\sim 17\,R_\odot$ is assumed. The black hole was schematically depicted as a black dot and the orbits are shown in red.

Procedure

The goal of the project, namely to set up a simple model of the wind dynamics in the Cygnus X-1 system, was achieved by proceeding as follows:

1. Introduction of gravitational potential

2. Distribution of "wind particles" on sphere around companion star's center of mass

3. Addition of an empirical model for the radiative pressure

4. Introduction of a toy model for photoionization

2.2 Integration Methods

Different integration methods were considered for the numerical determination of the "wind particle" behavior in the gravitational potential of the BH and O-star (see below). In order to test the different methods, the simple Kepler motion of the binary components was simulated and then compared to the analytical solution (see section 2.1) in each case. One has the following ordinary differential equations:

$$\frac{d\mathbf{x}_{\mathrm{bh}}}{dt} = \mathbf{v}_{\mathrm{bh}} \qquad\qquad \frac{d\mathbf{x}_{\star}}{dt} = \mathbf{v}_{\star} \qquad\qquad (2.5)$$

$$\frac{d\mathbf{v}_{\mathrm{bh}}}{dt} = \mathbf{a}_{\mathrm{bh}} = -G\frac{M_{\star}}{\left|\mathbf{x}_{\mathrm{bh}} - \mathbf{x}_{\star}\right|^{2}}\frac{\mathbf{x}_{\mathrm{bh}} - \mathbf{x}_{\star}}{\left|\mathbf{x}_{\mathrm{bh}} - \mathbf{x}_{\star}\right|} \qquad \frac{d\mathbf{v}_{\star}}{dt} = \mathbf{a}_{\star} = -G\frac{M_{\mathrm{bh}}}{\left|\mathbf{x}_{\star} - \mathbf{x}_{\mathrm{bh}}\right|^{2}}\frac{\mathbf{x}_{\star} - \mathbf{x}_{\mathrm{bh}}}{\left|\mathbf{x}_{\star} - \mathbf{x}_{\mathrm{bh}}\right|} \qquad (2.6)$$

If M_{bh} and $M_\star$ both lie on the x-axis for $t = 0$, one can express the initial values as (also see section 2.1)

$$\mathbf{x}_{\mathrm{bh}}(t = 0) = -\frac{1}{1+q} \begin{pmatrix} 1 \\ 0 \\ 0 \end{pmatrix} \qquad \mathbf{x}_\star(t = 0) = \frac{q}{1+q} \begin{pmatrix} 1 \\ 0 \\ 0 \end{pmatrix} \tag{2.7}$$

$$\mathbf{v}_{\mathrm{bh}}(t = 0) = -\frac{1}{1+q} \begin{pmatrix} 0 \\ 2\pi \\ 0 \end{pmatrix} \qquad \mathbf{v}_\star(t = 0) = \frac{q}{1+q} \begin{pmatrix} 0 \\ 2\pi \\ 0 \end{pmatrix} \tag{2.8}$$

The numerical integration of this initial value problem $y' = f(t, y)$, $y(t_0) = y_0$ was conducted with three different methods:

1. a simple 1st order integration:

$$y(t + dt) = y(t) + y'(t)dt \tag{2.9}$$

2. a 4th order Runge-Kutta integration (Press et al., 1992):

$$y_{n+1} = y_n + \frac{k_1}{6} + \frac{k_2}{3} + \frac{k_3}{3} + \frac{k_4}{6} + \mathcal{O}(h^5) \tag{2.10}$$

   where

$$k_1 = hf(t_n, y_n) \tag{2.11}$$

$$k_2 = hf(t_n + \frac{h}{2}, y_n + \frac{k_1}{2}) \tag{2.12}$$

$$k_3 = hf(t_n + \frac{h}{2}, y_n + \frac{k_2}{2}) \tag{2.13}$$

$$k_4 = hf(t_n + h, y_n + k_3) \tag{2.14}$$

   The method, leading to an error of the fifth order, thus uses four derivatives, one at the start- and endpoint as well as at two midpoints each (Press et al., 1992). Note that the basic Runge-Kutta method was employed and that no adaptive stepsize control was implemented in this case.

3. a 5th order Adams-Bashforth integration:
   When using the Adams-Bashforth method, the solution around t_n is approximated by (Butcher, 2003)

$$y_n = y_{n-1} + h(\beta_1 f(t_{n-1}, y_{n-1}) + \beta_2 f(t_{n-2}, y_{n-2}) + ... + \beta_k f(t_{n-k}, y_{n-k})). \tag{2.15}$$

   In the case of the 5th order method (i.e. the error is of 6th order), the β coefficients are

$$\beta_1 = \frac{1901}{720} \quad \beta_2 = -\frac{1387}{360} \quad \beta_3 = \frac{109}{30} \quad \beta_4 = -\frac{637}{360} \quad \beta_5 = \frac{251}{720}. \tag{2.16}$$

   Thus, unlike the Runge-Kutta method, which uses several midpoints between t_n and t_{n+1} to determine the approximated solution at t_{n+1}, Adams-Bashforth employs

the results of previous steps to arrive at the value for the next step ("multistep method"). Note that therefore in the case of Adams-Bashforth, when first starting the simulation, the values of f for the previous time steps have to be established with another method, in our case the 4th order Runge-Kutta method.

To compare the different integration methods, a measure for the deviation from the analytical Kepler solution was defined as

$$\Delta = \frac{\left|\mathbf{x}_{\mathrm{bh,numerical}} - \mathbf{x}_{\mathrm{bh,analytical}}\right| + \left|\mathbf{x}_{\star,\mathrm{numerical}} - \mathbf{x}_{\star,\mathrm{analytical}}\right|}{2}. \tag{2.17}$$

Figure 2 shows Δ for different stepsizes. For this kind of problem, the integration method with the highest order, the 5th order Adams-Bashforth integration, generally leads to the smallest deviation. When computing the motion of the binaries for up to 100 orbits, the 4th order Runge-Kutta method returned almost the same Δ up to a stepsize of ~ 0.01. The calculation time was not pivotal in the case of the presented simulations, though it was generally modest (minutes) even for several thousand particles (see next sections). All the following calculations were carried out with the 5th order Adams-Bashforth method.
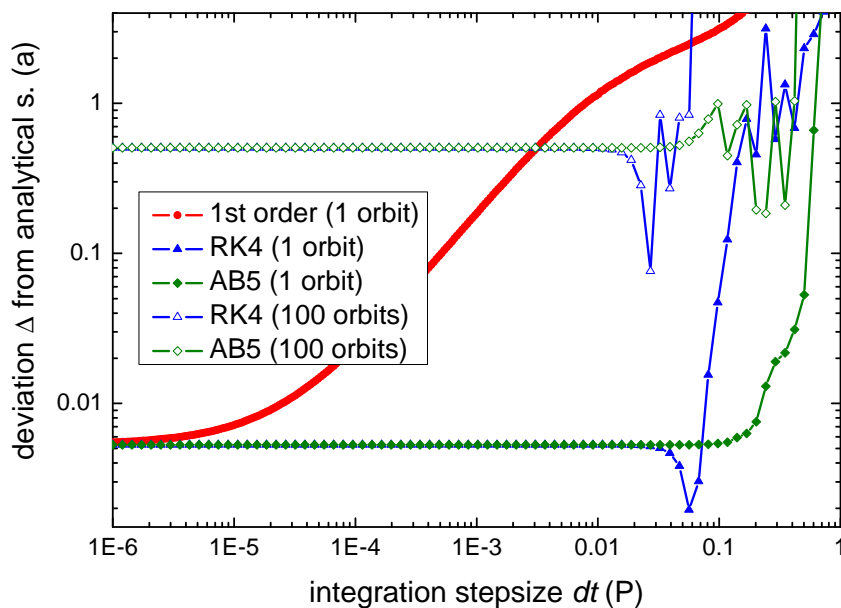
Figure 2: Deviation Δ from analytical solution (definition see text) at different stepsizes dt for the different integration methods. The blue and green curves show the deviation in the case of the 4th order Runge-Kutta and 5th order Adams-Bashforth methods, respectively. The solid symbols indicate the deviation after a single orbital period, the open symbols after 100 periods.

2.3 Wind Simulation

2.3.1 Initial Particle Distribution and Initial Velocity

In order to simulate the actual mass transfer, particles were placed uniformly on a sphere representing the companion star. These particles were assumed have a mass negligible compared to BH and star, and any interaction between them was ignored.

For a uniform placement on the sphere, a statistical distribution was used. At first, a systematic distribution similar to the system of latitudes and longitudes of the Earth's globe was considered. However, this would lead to a high particle concentration along the poles compared to the equator, thus this idea was quickly dismissed.

Let X_1 and X_2 be random numbers that are uniformly distributed in [0,1] (which can, e.g., be generated with S-Lang's `urand` function). Then define

$$\Theta = \arccos(2X_1 - 1) \tag{2.18}$$

$$\Phi = 2\pi X_2 \tag{2.19}$$

where (Θ, Φ) denotes the random point on the sphere. For a high number of particles, this statistical distribution leads to the same surface density in each $d\Omega$.

The motion of these particles in the gravitational potential of the BH and the companion star can then be described by the following set of ordinary differential equations. Note that the particle-sphere was set to have the same radius as the companion star, i.e. $R_\star \sim 17\,R_\odot$.

$$\frac{d\mathbf{x}_{\mathrm{par}}}{dt} = \mathbf{v}_{\mathrm{par}} \tag{2.20}$$

$$\frac{d\mathbf{v}_{\mathrm{par}}}{dt} = \mathbf{a}_{\mathrm{par}} = -G\left(\frac{M_{\mathrm{bh}}}{|\delta\mathbf{x}_{\mathrm{bh,par}}|^2}\frac{\delta\mathbf{x}_{\mathrm{bh,par}}}{|\delta\mathbf{x}_{\mathrm{bh,par}}|} + \frac{M_\star}{|\delta\mathbf{x}_{\star,\mathrm{par}}|^2}\frac{\delta\mathbf{x}_{\star,\mathrm{par}}}{|\delta\mathbf{x}_{\star,\mathrm{par}}|}\right) \tag{2.21}$$

where

$$\delta\mathbf{x}_{\mathrm{bh,par}} = \mathbf{x}_{\mathrm{bh}} - \mathbf{x}_{\mathrm{par}} \qquad \text{and} \qquad \delta\mathbf{x}_{\star,\mathrm{par}} = \mathbf{x}_\star - \mathbf{x}_{\mathrm{par}}. \tag{2.22}$$

The initial velocity of the particles was set to their orbital velocity around the common center of mass of the binary system. Along with the initial position, at the start of the integration one therefore has

$$\mathbf{x}_{\mathrm{par}}(t=0) = \mathbf{x}_\star + R_\star \begin{pmatrix} \sin\Theta\cos\Phi \\ \sin\Theta\sin\Phi \\ \cos\Theta \end{pmatrix} \tag{2.23}$$

$$\mathbf{v}_{\mathrm{par}}(t=0) = 2\pi \begin{pmatrix} -(\mathbf{x}_\star{}^{(2)} + R_\star\sin\Theta\sin\Phi) \\ \mathbf{x}_\star{}^{(1)} + R_\star\sin\Theta\cos\Phi \\ 0 \end{pmatrix}. \tag{2.24}$$

$\mathbf{x}_{\mathrm{bh}}$ and $\mathbf{x}_\star$ are the analytical solutions for the motion of the binary components' centers of mass (see Equations 2.3 and 2.4).

In this configuration, there is no equivalent for the star's gas pressure, causing the particles to fall towards the center of the star and actually to oscillate through it. For this reason, an initial radial velocity $v_{\text{radial}}(t = 0)$, pointing away from the center of the companion star, was added to Equation 2.24:

$$\mathbf{v}_{\text{par}}^{*}(t = 0) = 2\pi \begin{pmatrix} -(\mathbf{x}_{\star}^{(2)} + R_{\star} \sin \Theta \sin \Phi) \\ \mathbf{x}_{\star}^{(1)} + R_{\star} \sin \Theta \cos \Phi \\ 0 \end{pmatrix} + v_{\text{radial}}(t = 0) \begin{pmatrix} \sin \Theta \sin \Phi \\ \sin \Theta \cos \Phi \\ \cos \Theta \end{pmatrix} \quad (2.25)$$

For the speed of $v_{\text{radial}}(t = 0)$, a value around the escape velocity

$$|\mathbf{v}_{\star,\text{esc}}| = \sqrt{\frac{2GM_{\star}}{R_{\star}}} \approx 0.6 \times 10^3 \, \text{km s}^{-1} \quad (2.26)$$

was chosen to make up for the star's gas pressure (value for $R_{\star} \sim 17 \, R_{\odot}$, $M_{\star} \sim 17.8 \, M_{\odot}$). For details, see section 3.2.

2.3.2 Radiative Pressure

An aspect that has been entirely ignored so far, is the radiative pressure on the particles due to energized photons from the companion star. The radial velocity as a result of this pressure is often modeled (Lamers & Leitherer, 1993) as

$$v_{\text{radiative}}(r) = v_0 + (v_{\infty} - v_0) \left(1 - \frac{R_{\star}}{r}\right)^{\beta}. \quad (2.27)$$

After Herrero et al. (1995), $v_{\infty} \sim 2100 \, \text{km s}^{-1}$ was assumed. The exponent β was set to a value around 1 and v_0 to a value close to zero, in agreement with Friend & Castor (1983) who suggest that $v_{\text{radiative}}(r)$ is approximately $v_{\text{radiative}}(r) = v_{\infty}(1 - R_{\star}/r)$ for early-type stars (HDE 226868 is an O-star).

The radiative acceleration on the particles is then given by

$$a(r) = \frac{dv}{dt} = \frac{dv}{dr}\frac{dr}{dt} = \beta \left(v_{\infty} - v_0\right) \left(1 - \frac{R_{\star}}{r}\right)^{\beta-1} \frac{R_{\star}}{r^2} \cdot v(r). \quad (2.28)$$

When comparing the effect resulting from the radiative pressure to the gravitational acceleration due to BH and companion star, the latter can be almost entirely ignored (see Figure 7) . However, when the ionization of the wind particles due to an intense X-ray flux close to the BH is taken into account, the radiative effect becomes less dominant (see next section and discussion).

2.3.3 Photoionization

Finally, we tried to investigate the effects of photoionization within this simplified model. According to an idealized model by MacGregor & Vitello (1982), a high X-ray emission, produced close to the BH, could decrease the radiation force affecting the wind. They

Figure 3: Scaling factor c of the radiative acceleration as a function of the distance from the BH (unit a: distance BH-secondary center). The ionization distance r_{ion}, at which the radiative acceleration is abruptly changing in the model, was set to 0.4. The "softness" of the transition is $\Delta = 0.05 \ll 1$.
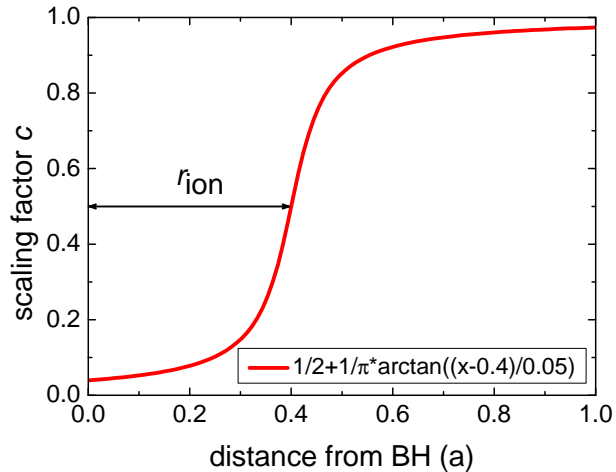
suggest that for secondaries with a very high X-ray luminosity, the lower stages of ionization are less abundant in the radiation-driven wind and the optical line depth increases, leading to smaller velocities. Gies et al. (2003) describe a possible anti-correlation between a high ionization due to hard X-rays and a low velocity of the wind in the case of the Cygnux X-1/ HDE226868 system. Blondin (1994) attributes this to a decrease in the effect of the radiative pressure by the UV photons from the blue supergiant onto the wind.

In the model under discussion, a scaling factor c was added to Equation 2.28 in order to very roughly account for the effect of a decreased radiative pressure due to photoionization. Depending on the distance of the particles from the BH, this coefficient leads to a reduction of the acceleration due to the radiative pressure. Different possibilities to describe the ionization's dependency on the BH-particle distance in the model were considered. In the end, it was decided to choose a model that assumes an almost complete particle-ionization up to a certain distance r_{ion}, at which it abruptly declines. This was done by scaling the radiative acceleration with an arctan-function

$$c = \frac{1}{2} + \frac{1}{\pi} \arctan \left(\frac{r_{\mathrm{bh\text{-}particle}} - r_{\mathrm{ion}}}{\Delta} \right) \tag{2.29}$$

where $r_{\mathrm{BH\text{-}particle}}$ is the distance between the respective wind particle and the BH and r_{ion} is the distance from the BH at which the ionization abruptly declines in the model. Δ is the factor describing the "softness" of the transition between the fully ionized zone and the area where the radiative acceleration is almost undiminished. In the following, Δ will be $\ll 1$, thereby assuming a relatively abrupt reduction in the ionization at r_{ion}.

3 Results and Discussion

3.1 Particle Distribution

For the purpose of quantitatively determining the particle distribution after successively accounting for different effects in the simulation, a histogram-method was introduced. The number of particles was determined along with their distance from the BH along the line of sight to the observer, assuming an inclination of $i = 35°$ (Herrero et al., 1995).
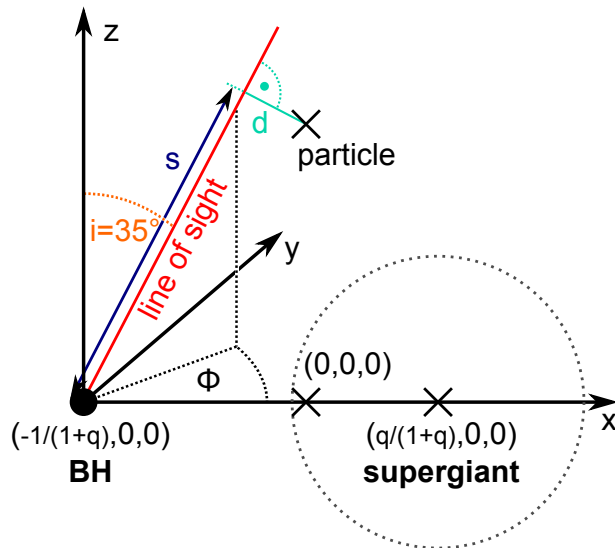
Figure 4: Schematic view of the line of sight as it was modeled in the simulation (co-rotating frame of reference). d is the shortest distance between a particle and the line of sight (LOS). The distance between the point on the LOS closest to the particle and the BH, s, is used to quantitatively describe the particle distribution in the simulation (see text).

More quantitatively speaking, a particle $\mathbf{x}_{par} = (x_{par}(t), y_{par}(t), z_{par}(t))$ is counted as follows: When one makes the simplification of setting the azimuthal angle in the x-y plane to zero for all orbital phases, the line of sight with regard to the BH (also see Figure 4) can be parametrized as

$$\mathbf{r}_{LOS} \overset{obs}{=} -\frac{1}{1+q} \begin{pmatrix} \cos 2\pi t \\ \sin 2\pi t \\ 0 \end{pmatrix} + a \begin{pmatrix} 1 \\ 0 \\ (\tan i)^{-1} \end{pmatrix} \tag{3.1}$$

$$\overset{co\text{-}rot}{=} -\frac{1}{1+q} \begin{pmatrix} 1 \\ 0 \\ 0 \end{pmatrix} + a \begin{pmatrix} \cos 2\pi t \\ -\sin 2\pi t \\ (\tan i)^{-1} \end{pmatrix} \tag{3.2}$$

where the first and second line give $\mathbf{r}_{LOS}$ in the case of the observer's frame and a co-rotating frame of reference, respectively. $\phi = 2\pi t$ is the relative angle between the binary axis and the line of sight, i denotes the inclination of the system's orbital plane and a is a scalar multiple of the distance from the BH.

Furthermore, one can define

$$d = |\mathbf{x}_{par} - \mathbf{r}_{LOS}(a^\star)| \tag{3.3}$$

$$s = |\mathbf{r}_{LOS}(a^\star) - \mathbf{x}_{bh}| \tag{3.4}$$

where $a^\star$ is the scalar multiple, for which $d = |\mathbf{x}_{\mathrm{par}} - \mathbf{r}_{\mathrm{LOS}}(a^\star)| = \min_a |\mathbf{x}_{\mathrm{par}} - \mathbf{r}_{\mathrm{LOS}}(a)|$ (see Figure 4) and where $\mathbf{x}_{\mathrm{bh}}$ is the BH position. s is the distance between the BH and the point where the LOS is closest to the particle, and will be used to determine the particle distribution along the LOS.

By making use of those definitions, it is possible to visualize the particle distribution at a certain time step t_j in a histogram, in which an individual bin $h_i(t_j)$ is given by

$$h_i(t_j) = \text{number of particles with } s_i \leq s(x_{\mathrm{par}}) < s_{i+1} \text{ and } d(x_{\mathrm{par}}) \leq 0.2. \tag{3.5}$$

In the case of the histograms shown, the bin size $s_i - s_{i+1}$ was 0.01 and only particles up to two orbital distances from the BH were considered. Furthermore, instead of showing the particle distribution for a certain t_j, the histograms in the following figures sum up the distributions at all time steps of the simulation. The bins of these time-independent histograms are therefore defined as

$$h_i^\star = \sum_j h_i(t_j). \tag{3.6}$$

The summing up is necessary because in the simulation, wind particles are only spawned at the first time step, i.e. only once. Instead of simulating a continuous wind flow by "generating" new particles at the star's surface at each t_j, one can just as well add up the time-dependent distributions of one set of particles.

In the following histograms, the time steps up to 0.1 orbital periods were considered in calculating $h_i^\star$. At this value, the particles were generally far outside of the vicinity of star and BH. In the presence of radiative pressure, almost no particles are left at distances < 1 a after ~ 0.05 orbital periods.

To evaluate the wind particle distribution in different regions around the BH, the histograms were determined along the lines of sight at four fixed angles $(0°, 90°, 180°, 270°)$ with respect to the binary axis.

3.2 Initial Velocity

As mentioned in section 2.3.1, the particles had to be given an initial velocity to make up for the lack of the star's gas pressure in the simulation. In section 2.3.1, it was suggested that a value roughly around the escape velocity $|\mathbf{v}_{\star,\mathrm{esc}}| \approx 0.6 \times 10^3 \, \mathrm{km\,s^{-1}}$ might be reasonable. This shall be elaborated on and specified more in the following.

Figure 5 shows the particle distribution along the line of sight (see section 3.1) for an angle of $\phi = 0°$ with respect to the binary axis and for different initial velocities. For relatively high initial speeds $v_{\mathrm{start}} = 800 \, \mathrm{km\,s^{-1}}$ and $v_{\mathrm{start}} = 1000 \, \mathrm{km\,s^{-1}}$, the particles reach the vicinity of the line of sight quickly and generally cross it at larger distances from the BH than particles starting slower. However, fewer of these high-speed particles are kept close to the BH due to its gravitational acceleration than their low-speed counterparts.
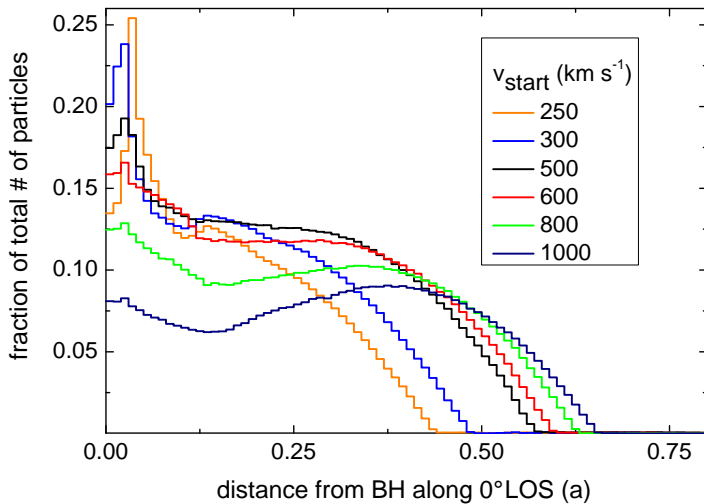
Figure 5: Particle distribution along the line of sight at 0° with respect to the binary axis for different initial velocities. The simulations were carried out for 10^5 particles and for a length of 0.1 orbital periods (5th order Adams-Bashforth, $dt = 4 \times 10^{-4}$).

Particles with smaller initial speeds of $v_{\mathrm{start}} = 600\,\mathrm{km\,s^{-1}}$ and lower are more likely to reach the vicinity of the BH. Note, however, that for $v_{\mathrm{start}} = 250\,\mathrm{km\,s^{-1}}$, despite the lower speed, only a smaller part of the total number of particles was fully drawn into the gravitational potential of the BH than in the case of e.g. $v_{\mathrm{start}} = 300\,\mathrm{km\,s^{-1}}$. Many particles almost reach the BH, but are then accelerated back to the star, where they "oscillate" through the center of mass due to a numerical artifact (see below). In Figure 5 this becomes evident when looking at the distribution for $v_{\mathrm{start}} = 250\,\mathrm{km\,s^{-1}}$ (orange line), which peaks at a BH-distance of slightly below 0.05 and abruptly decreases for greater and smaller values. For very small initial speeds below $200\,\mathrm{km\,s^{-1}}$, the sphere of particles cannot escape from the gravitational potential of the secondary and collapses towards the star's center of mass, which in turn leads to an ejection of the particles into random directions due to a numerical artifact (see Figure 6a).

The mentioned "oscillations" are an artifact of the simulation which does not take into account the star's gas pressure. When the particles get very close to the center of mass, the problem is exacerbated by an acceleration of the particles in random directions, an artifact of the integration method. Since the initial radiative velocities in this section were introduced precisely because we wanted to make up for the absence of the star's gas pressure in the simulation, it was necessary to use values above $\sim 250\,\mathrm{km\,s^{-1}}$ for v_{start} in order to avoid those artifacts.

Finally note that in the simulation, values of 300 to $500\,\mathrm{km\,s^{-1}}$ led to a slightly higher fraction of the particles entering the sphere with radius 0.1 around the BH than the escape velocity of $|\mathbf{v}_{\star,\mathrm{esc}}| \approx 0.6 \times 10^3\,\mathrm{km\,s^{-1}}$.

3.3 Radiative Pressure

Radiative acceleration was applied to the particles in a next step, simulated as described in section 2.3.2. A first finding was that this radiative acceleration is generally much stronger than the gravitational acceleration due to the star's and the BH's masses. The

(a) $v_{start} = 100\,\mathrm{km\,s^{-1}}$
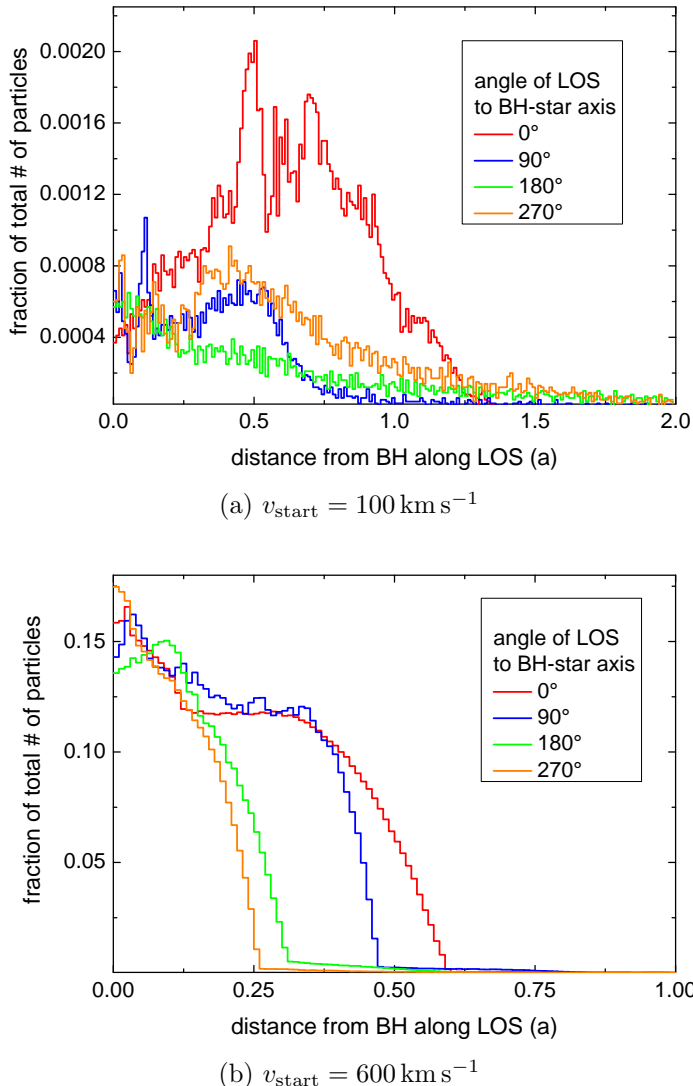
(b) $v_{start} = 600\,\mathrm{km\,s^{-1}}$

Figure 6: Particle distributions for (a) $v_{start} = 100\,\mathrm{km\,s^{-1}}$ and (b) $600\,\mathrm{km\,s^{-1}}$, respectively. The distributions were determined along the lines of sight for four fixed angles ϕ with regard to the binary axis ($\phi = 0°, 90°, 180°, 270°$). 10^5 particles were used and a duration of 0.1 orbital periods was examined (5th order Adams-Bashforth, $dt = 4 \times 10^{-4}$).

initial velocity discussed in the previous section is therefore no longer necessary as there is no risk of the particles being pulled back to the star's center of mass. Nevertheless, a small value of several $\mathrm{km\,s^{-1}}$ for the initial velocity was retained instead of completely eliminating the v_{start}-term: It moves the particles *slightly* away from their initial position at $R_\star$ around the star into the radiative acceleration field where $a_{radiative}(r) \gg a_{\star,gravitation}(r)$ (see Figure 7).

The strong radiative acceleration also leads to a much smaller fraction of particles being drawn into the vicinity of the BH by its gravitational force. Thus, a short calculation was carried out to see whether the "accreted" proportion of the wind in this simulation would be high enough to cause the X-ray luminosity observed in reality.

Assuming an X-ray luminosity of $\sim 10^{38}\,\mathrm{erg\,s^{-1}}$ (Hanke, 2010, priv. comm.) and an accretion efficiency of $E = 0.1\,mc^2$ (Narayan & Quataert, 2005), one gets that an accretion mass of around $1.8 \times 10^{-8}\,M_\odot$ is needed in a year to bring about the BH's luminosity.
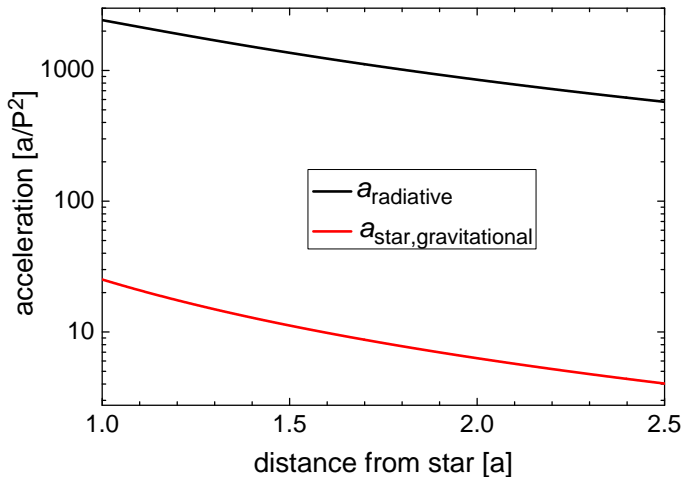
Figure 7: Acceleration due to radiative pressure and gravitational attraction of the star as a function of the distance from the star's center of mass (see Equations 2.28 and 2.21). Photoionization and the gravitational potential of the BH were ignored.

Literature suggests that a mass loss rate of $\sim 3 \times 10^{-6} \, M_\odot \, \mathrm{yr}^{-1}$ (Herrero et al., 1995) for HDE 226868 is reasonable. That means that

$$\eta \sim \frac{1.8 \times 10^{-8} \, M_\odot \, \mathrm{yr}^{-1}}{3 \times 10^{-6} \, M_\odot \, \mathrm{yr}^{-1}} = 5.8 \times 10^{-3} \tag{3.7}$$

of the wind is accreted. In the simulation, the fraction of the total number of particles passing through a sphere with a radius of 0.05 around the BH is $\eta_{\mathrm{rad, \, simulation}} = 3.24 \times 10^{-3}$. If one assumes that this is the "accreted" wind proportion, admittedly a strong assumption, then the value in the simulation is of the same order as η in Equation 3.7 (in the absence of any gravitational acceleration, $\eta_{\mathrm{rad, \, simulation}}$ would be about an order of magnitude lower). Therefore, the radiative acceleration, modeled as described in section 2.3.2, would provide roughly the mass needed to feed the X-ray luminosity of the compact object.

Note, however, that this statement is undermined by the choice of the radius around the BH to determine the fraction of "accreted" wind particles in the simulation. The chosen value of 0.05 is fairly large and therefore, the "accretion rate" in the simulation might even be smaller than the $\eta_{\mathrm{rad, \, simulation}}$ given above. As it will be shown in the following section, this might be compensated by photoionization, which has not yet been accounted for.

3.4 Ionization

Returning to the assumption that the ionization of particles as a function of the distance from the BH can be described by Equation 2.29, the problem of choosing the right parameters remains. Regarding the ionization distance r_{ion}, one has to consider three main cases (where $R_\star$ is the radius of the star):

1. $r_{\mathrm{ion}} \ll (1.0 - R_\star)$: When the ionization zone around the BH is set to be small, the fraction of particles reaching the vicinity of the BH is similar to the one in the case with radiative pressure only (see section 3.3). This becomes evident in Figure 9, where the particle distribution for $r_{\mathrm{ion}} = 0.3$ (blue curve) is almost identical to the
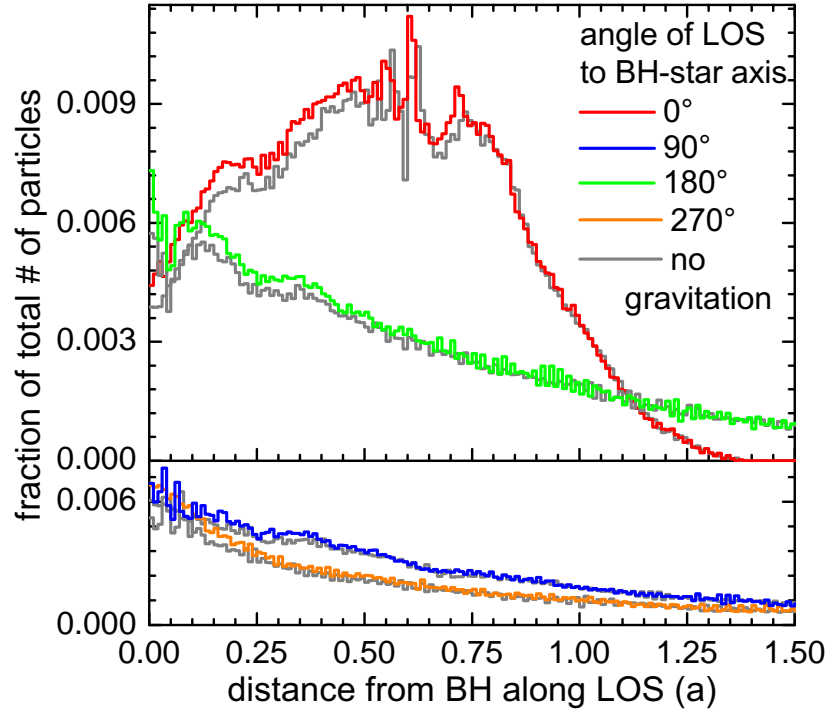
Figure 8: Particle distribution in the presence of radiative pressure (see text). The distri-
bution was determined along the line of sight for four fixed angles ϕ with regard to the
binary axis ($\phi = 0°, 90°, 180°, 270°$). Because of the high radiative acceleration, the
particles are almost isotropically spread in all directions and resemble the distribution
in the absence of any gravitational acceleration by BH and star (grey curves). Like
previously, the simulations were carried out for 10^5 particles and for a length of 0.1
orbital periods (5th order Adams-Bashforth, $dt = 4 \times 10^{-4}$).

calculated distribution in the absence of any photoionization (red curve,Figure 8).
Presumably, this is due to the fact that the particles experience a strong radiative
acceleration when still close to the supergiant. Once they enter the photoionization
zone, they already have high velocities and therefore the effect of photoionization is
low.

2. $r_{\mathrm{ion}} \approx (1.0 - R_\star)$: When the ionization sphere with radius r_{ion} includes the particles'
   initial position, the latter experience the radiative pressure of the star only very
   briefly (depending on Δ, the "softness" of the transition to the fully ionized zone,
   see Equation 2.29). Therefore, their velocity is still relatively small and they stay
   in the immediate gravitational field of the BH for a longer timespan than in the
   case where $r_{\mathrm{ion}} \ll (1.0 - R_\star)$. This directly leads to a higher fraction of "accreted"
   particles, which becomes evident when looking at the green, orange and grey curves
   ($r_{\mathrm{ion}} = 0.6, 0.7, 0.8$) in figure 9, respectively. They indicate that for the choice of

$r_{\text{ion}} \approx (1.0 - R_\star)$ the fraction of wind particles reaching the vicinity of the BH is several times larger than the one in the case of smaller and larger r_{ion}.

3. $r_{\text{ion}} \gg (1.0 - R_\star)$: When the ionization sphere is set to include the largest part of the star or even the whole supergiant, the particles are exposed (almost) exclusively to the gravitational force of BH and star. The arctan function in Equation 2.29 denotes the radiative pressure with a weight factor $c \approx 0$, so that the radiative acceleration of the particles can be ignored in the vicinity of the star and BH. The behavior of the particles for $r_{\text{ion}} = 1.0$ (dark yellow) and especially for $r_{\text{ion}} = 1.5$ (red) in Figure 9 is therefore similar to the distribution in the case of low initial velocities in section 3.2 (see Figure 6a).

Obviously, both the first case (photoionization almost negligible) and the last case (absence of radiative pressure and no wind from the star) are not in accordance with physics or the scientific consensus on the wind dynamics of Cygnus X-1.
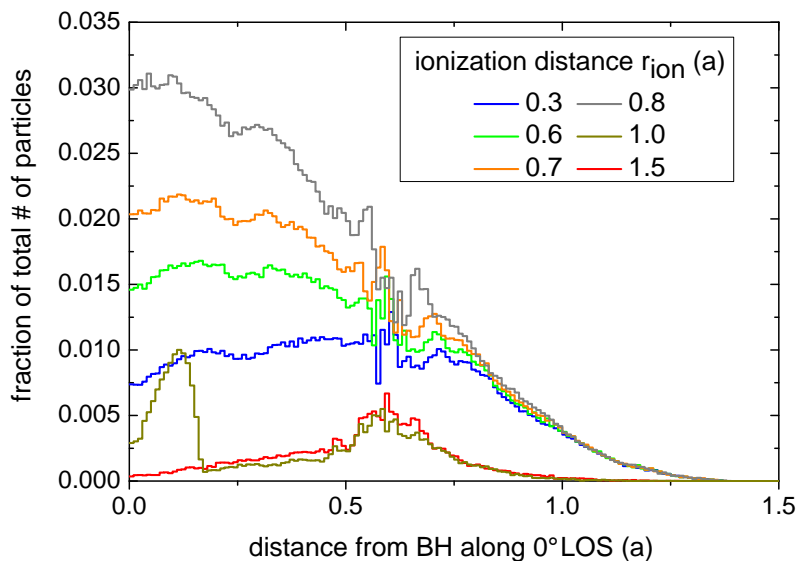
Figure 9: Particle distribution in the presence of photoionization and radiative pressure for different ionization distances r_{ion} (see section 2.3.3). In each case, the particle distribution was determined along the line of sight at an angle of $0°$ with regard to the binary axis. 10^5 particles were used and a duration of 0.1 orbital periods was considered (5th order Adams-Bashforth, $dt = 4 \times 10^{-4}$).

It is therefore necessary to have a closer look at the second case, where $r_{\text{ion}} \approx (1.0 - R_\star)$, i.e., where the ionization sphere extends roughly from the BH to the star's surface. In this case, a fraction of $\eta_{\text{ion, simulation}} = 4.4 \times 10^{-3}$, 1.1×10^{-2} and 1.3×10^{-2} of the particles reaches a sphere with radius 0.05 around the BH for $r_{\text{ion}} = 0.6$, 0.7 and 0.8, respectively (if the transition "softness" $\Delta = 0.2$). In comparison to the case with radiative pressure but without photoionization ($\eta_{\text{rad, simulation}} = 3.24 \times 10^{-3}$), the "accreted" fraction of particles is up to four times higher. For an X-ray luminosity of $\sim 10^{38}\,\text{erg}\,\text{s}^{-1}$, roughly 5.8×10^{-3}

of the wind needs to be accreted (section 3.3). Therefore, when making the very strong simplification that a particle in the simulation counts as "accreted" once it enters the sphere of radius 0.05 around the BH, an ionization radius of $r_{\mathrm{ion}} \sim 0.6$ seems to be the most reasonable choice.

While it was possible to include a model for photoionization into this simple simulation, one of its major shortcomings is the lack of any interaction between the individual particles. This makes the formation of an accretion disk impossible – it would require friction to take place which is not accounted for in the simulation.

4 Conclusion

The wind dynamics in the X-ray binary system Cygnus X-1/ HDE 226868 was modeled by gradually expanding a simple simulation to account for different effects, namely gravitational acceleration, the star's radiative pressure and ionization due to the BH's strong X-ray flux. To look at the physics behind the simulation, the wind particle distribution along the line of sight at different angles with regard to the binary axis was examined in each step. The simulations were carried out for 10^5 non-interacting particles using the 5th order Adams-Bashforth integration method.

In particular, the following points deserve special mentioning:

1. If only the gravitational acceleration due to BH and star is considered, the wind particles, initially placed at the star's surface, need to have a radial start velocity slightly below the theoretical escape velocity $|\mathbf{v}_{\star,\mathrm{esc}}| \approx 0.6 \times 10^3\,\mathrm{km\,s^{-1}}$. This is necessary to make up for the lack of the star's gas pressure in the simulation.

2. Generally speaking, the acceleration of the particles due to the radiative pressure of the star ($a_{\mathrm{radiative}}(r) = dv_{\mathrm{radiative}}/dt$ where $v_{\mathrm{radiative}}(r) = v_0 + (v_\infty - v_0)(1 - R_\star/r)^\beta$) is much larger than the gravitational acceleration towards BH and star.

3. The fraction of particles accreted by the BH in the presence of radiative pressure, $\eta_{\mathrm{rad,\ simulation}} = 3.24 \times 10^{-3}$, is slightly smaller, but of the same order as the fraction needed to roughly account for the BH's X-ray luminosity, $\eta \sim 5.8 \times 10^{-3}$.

4. If a photoionization sphere of radius r_{ion} is considered, inside of which the radiative pressure is set approximately to zero, then the value of r_{ion} must be chosen neither too small (almost no effect) nor too large (radiative pressure negligible near star and BH). Therefore, an ionization radius r_{ion} that is roughly equal to the distance between BH and the star's surface seems to be a reasonable choice. In this case, the fraction of the wind particles accreted by the BH is close to the value needed to explain the X-ray luminosity of Cygnus X-1.

References

Blondin J.M., 1994, ApJ 435, 756

Bolton C.T., 1972, Nat 235, 271

Bolton C.T., 1975, ApJ 200, 269

Bowyer S., Byram E.T., Chubb T.A., Friedman H., 1965, Science 147, 394

Butcher J., 2003, Numerical methods for ordinary differential equations, Numerical algorithms, J. Wiley

Cowley A.P., 1992, ARA&A 30, 287

Frank J., King A., Raine D., 2002, Accretion power in astrophysics, Cambridge University Press

Friend D.B., Castor J.I., 1982, ApJ 261, 293

Friend D.B., Castor J.I., 1983, ApJ 272, 259

Gies D.R., Bolton C.T., 1982, ApJ 260, 240

Gies D.R., Bolton C.T., Blake R.M., et al., 2008, ApJ 678, 1237

Gies D.R., Bolton C.T., Thomson J.R., et al., 2003, ApJ 583, 424

Hanke M., 2011, Ph.D. thesis, Dr. Karl Remeis-Sternwarte and Erlangen Centre for Astroparticle Physics, Friedrich-Alexander-Universität Erlangen-Nürnberg

Hanke M., Wilms J., Nowak M.A., et al., 2009, ApJ 690, 330

Herrero A., Kudritzki R.P., Gabler R., et al., 1995, A&A 297, 556

Houck J.C., Denicola L.A., 2000, In: N. Manset, C. Veillet, & D. Crabtree (ed.) Astronomical Data Analysis Software and Systems IX, Vol. 216. Astronomical Society of the Pacific Conference Series, p.591

Israel G.L., 1996, Ph.D. thesis, Osservatorio Astronomico di Roma, Trieste

Janka H.T., Kifonidis K., Rampp M., 2001, In: D. Blaschke, N. K. Glendenning, & A. Sedrakian (ed.) Physics of Neutron Star Interiors, Vol. 578. Lecture Notes in Physics, Berlin Springer Verlag, p.333

Kühnel M., 2011, *Master's thesis*, Dr. Karl Remeis-Sternwarte and Erlangen Centre for Astroparticle Physics, Friedrich-Alexander-Universität Erlangen-Nürnberg

Lamers H.J.G.L.M., Leitherer C., 1993, ApJ 412, 771

MacGregor K.B., Vitello P.A.J., 1982, ApJ 259, 267

Narayan R., Quataert E., 2005, Science 307, 77

Press W.H., Flannery B.P., Teukolsky S.A., Vetterling W.T., 1992, Numerical Recipes in C: The Art of Scientific Computing, Second Edition, Cambridge University Press, 2 edition

Schatz H., Rehm K.E., 2006, Nuclear Physics A 777, 601

Webster B.L., Murdin P., 1972, Nat 235, 37

Erklärung

Ich versichere, dass ich die Arbeit ohne fremde Hilfe und ohne Benutzung anderer als der angegebenen Quellen angefertigt habe und dass die Arbeit in gleicher oder ähnlicher Form noch keiner anderen Prüfungsbehörde vorgelegen hat und von dieser als Teil einer Prüfungsleistung angenommen wurde. Alle Ausführungen, die wörtlich oder sinngemäß übernommen wurden, sind als solche gekennzeichnet.

Osaka, den 1.10.2011

Acknowledgments